energies

MDPI

Article

On the Compatibility of Electric Equivalent Circuit Models for Enhanced Flooded Lead Acid Batteries Based on Electrochemical Impedance Spectroscopy

Can Aksakal [1,2] and Altug Sisman [1,*]

[1] Energy Institute, Istanbul Technical University, 34469 Istanbul, Turkey; aksakal@itu.edu.tr
[2] INCI GS YUASA, 45030 Manisa, Turkey
* Correspondence: sismanal@itu.edu.tr; Tel.: +90-212-285-3884

Received: 8 December 2017; Accepted: 31 December 2017; Published: 3 January 2018

Abstract: Electric equivalent circuit (EEC) models have been widely used to interpret the inner dynamics of all type of batteries. Added to this, they also have been used to estimate state of charge (SOC) and state of health (SOH) values in combination with different methods. Four EEC models are considered for enhanced flooded lead acid batteries (EFB) which are widely used in micro hybrid vehicles. In this study, impedance and phase prediction capabilities of models throughout a frequency spectrum from 1 mHz to 10 kHz are compared with those of experimental results to investigate their consistency with the data. The battery is charged, discharged, and aged according to appropriate standards which imitates a lifetime of a micro hybrid vehicle battery under high current partial cycling. Impedance tests are repeated between different charge and health states until the end of the battery's lifetime. It is seen that adding transmission line elements to mimic the high porous electrode electrolyte interface to a double parallel constant phase element resistance model (ZARC) can increase the model data representing capability by 100%. The mean average percentage error (MAPE) of the conventional model with respect to data is 3.2% while the same value of the transmission line added model found as 1.6%. The results can be helpful to represent an EFB in complex simulation environments, which are used in automobile industry.

Keywords: micro-hybrid vehicles; lead acid battery; enhanced flooded battery; impedance spectroscopy; state of charge; state of health

1. Introduction

Vehicle emission regulations have been forcing the automotive industry worldwide to reduce its carbon footprint [1]. Environmentally friendly, full electric and plug-in hybrid vehicles are gaining popularity and their sales numbers increase each year but due to limited sales volumes, their effect on fleet emission reduction is limited. The trend in the mass market is also progressing in the same direction and as a result, fuel efficient micro-hybrid vehicle sales are also gaining popularity. According to market research, total micro-hybrid vehicle sales will increase from 8.8 million in 2013 to 55.3 million in 2022 [2]. Lead-acid batteries are still unrivaled for micro-hybrid vehicles as well as conventional vehicles due to their robust and safe design, low cost raw materials, mature and cost optimized manufacturing process, and already established efficient recycling processes [3,4]. A lead acid car battery designed for a micro-hybrid vehicle should have additional duties over a standard battery designed only for starting, lighting, and ignition (SLI) applications. A micro-hybrid vehicle battery should be able to supply energy during idle engine stop periods. It can be charged at high current rates during regenerative braking or even it may help the engine to boost acceleration via alternator/generator. To achieve these new duties, some breakthrough improvements have been adapted to lead acid batteries. Newly developed carbon additives have been applied to negative

electrodes to increase the cyclic ability and dynamic charge acceptance [5,6]. Electrode grids have been designed with computer aided optimization techniques to minimize voltage loss at high current rates without increasing the grid weight [7]. High porous and low tortuous separators with low electric resistances are now commercially available and they have been utilized in lead acid batteries to improve their electrical performance such as increased cyclic endurance and higher dynamic charge acceptance. These new type lead acid batteries are called enhanced flooded batteries (EFB) [8–10]. EFB can last much longer than that of regular flooded lead acid batteries under high electrical stress of micro-hybrid vehicles. Unlike conventional vehicles, micro-hybrid vehicles utilize lead-acid batteries in a partial state of charge (SOC) to capture energy during the regenerative braking. The electronic control unit of the micro hybrid vehicle should know the battery SOC to decide to stop the engine or not and to decide the charging current during deceleration. Therefore, in recent studies rival lead acid battery technologies have been focusing to understand the SOC of the battery inside the micro hybrid vehicles [11]. In the lifetime of a lead acid battery, various electrochemical degradation processes like sulphation, acid stratification, grid corrosion, etc. could occur. These degradation processes can result in changes in the crystallographic structure of battery materials, influencing electrode potentials. Thus, it usually misleads the end user or car electronic control unit to get an idea about exact SOC and SOH from open circuit voltages. In literature, there are numerous studies that explain electrochemical degradation processes of a lead acid battery [12] and for other chemistries [13–15] to understand their SOC and SOH levels. Most of these works are based on highly non-linear and complex equations based on the underlying physics of an electrochemical cell. Usually these models need more time to simulate. If there is a need of SOC or SOH information in a real time simulation faster methods become a necessity.

Electrochemical impedance spectroscopy (EIS) is a faster technique that has a potential to identify the SOC and SOH of a lead acid battery if data sets have been interpreted with a convenient electric equivalent circuit (EEC) model. Besides SOC and SOH predictions, another reason to use an EEC for energy storage unit of an automobile has emerged in recent years. Batteries are increasingly incorporated into the complex electronic system of a car as hybrid powertrain systems are getting more complicated. The resulting electronic and electrochemical combined systems need to be analyzed as a whole. EEC is an easier and efficient way of representing a battery which is in interaction with other electronic components of a hybrid powertrain in a simulation environment [16]. In this paper, the precisions of previously proposed and commonly used EEC models of lead acid batteries are experimentally investigated for modern enhanced flooded batteries, which are widely using in today's conventional vehicles.

In their early work, Gopikanth and Sathyanamara [17] examined the dependency of the impedance data with respect to SOC for a lead acid battery in a relatively narrow frequency spectrum range. They observed that above 200 Hz, the inductive behavior becomes prominent and decided to concentrate on the range between 100 Hz to 15 Hz. In this range, change in the quantities of electrical elements have been observed with respect to SOC. Due to the parabolic behavior of elements, using these parameters for SOC predictions are found as a limited indicator. Mauracher and Karden [18] have completed a series of EIS tests on lead acid batteries to identify parameters of their EEC battery model based on Randles theory. Their proposed model can give battery terminal voltage as a function of current without taking into account of temperature, SOC and SOH with 0.2% voltage tolerance on their simulations. Blanke and co-workers [19] showed that higher frequency region could also give valuable information on SOC. For a certain frequency, the mixed inductive and capacitive behaviors of a lead acid battery cancel each other and the imaginary part of impedance becomes zero for a given SOC value. This frequency is named as transition frequency (F_{Tr}). They observed that this parameter is highly dependent on SOC and the temperature of the battery. Impedance data are shown in Bode or in Nyquist diagrams. In former one, modulus of real and imaginary parts and phase angle are given with respect to frequency in log scale. In the latter case, the negative values of imaginary impedance

are shown with respect to real impedances to have capacitive loops in the upper part of the graph. An idealized shape of a Nyquist diagram for a lead acid battery is given in Figure 1 below.

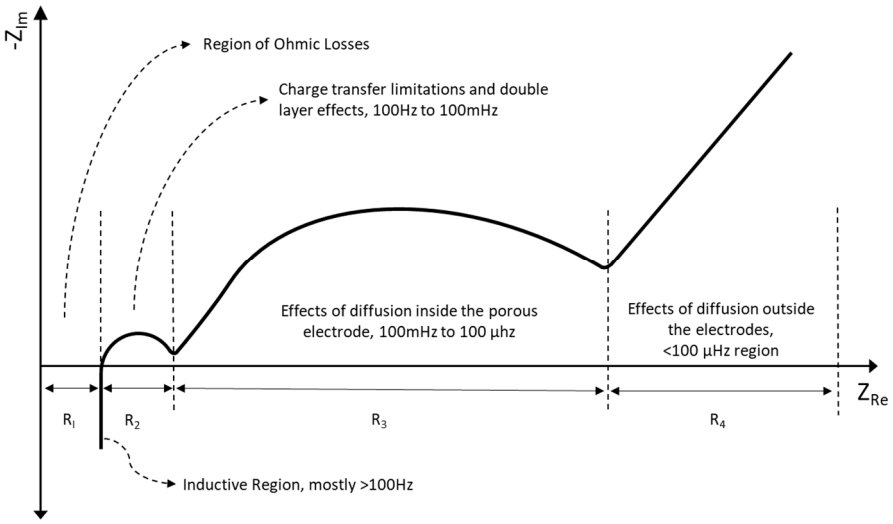

Figure 1. Shape of an idealized Nyquist diagram for lead acid battery.

In this work, impedance spectrum analyses on an EFB are performed for a wide SOC and SOH ranges. To interpret impedance data, widely used double ZARC element model is modified by adding transmission line elements to each ZARC for an EFB for the first time. This new model is also compared with three existing models from literature.

Experiments are conducted under zero DC without discharging or charging to avoid SOC changes during the EIS measurement. Charge, discharge, and cycling procedures of European Committee for Electrochemical Standardization (CENELEC) [20,21] are applied to the battery to change its SOC and SOH. Rather than charging and discharging with a big depth of discharge to aging the battery, these standards designed for micro hybrid vehicle batteries can imitate the real-life working conditions. An equivalent circuit with only simple electrical elements [22,23], a typical Randles circuit with an addition of inductance [24], a model with two constant phase elements (CPE) in parallel with resistances [19,25], and finally a circuit with addition of two transmission line elements representing for both anode and cathode porous electrode surfaces are considered to investigate their consistency with experimental data.

Before investigating a relationship between data and introduced models, a data quality analysis method called Kramers-Kronig (KK) is used to be sure that data are linear, causal and stable thus self-consistent [26]. KK relation dictates that real and imaginary parts of any immittance function are interdependent based on following equations:

$$Z_{Im}(\omega) = \frac{2\omega}{\pi}\int_0^\infty \frac{Z_{Re}(x) - Z_{Re}(\omega)}{x^2 - \omega^2}dx \quad (1)$$

$$Z_{Re}(\omega) = R_\infty + \frac{2}{\pi}\int_0^\infty \frac{xZ_{Im}(x) - \omega Z_{Im}(\omega)}{x^2 - \omega^2}dx \quad (2)$$

Following the KK data validation, a software based on simplex algorithm is used to change model parameters to minimize the chi-square (χ^2) value of the model with data. Model accuracies with respect to data are analyzed based on MAPE method for different SOC and SOH conditions. It is shown that a circuit with additional transmission line elements has the minimum error in comparison with measurements for the full range of SOC and SOH. Also, it is seen that the precisions of the models can be different for real and imaginary parts of impedance as well as the phase shift.

2. Experimental Setup, Procedures, and Results

EIS tests, SOC adjustments, and cycling procedure to aging the battery are realized on the same experimental setup shown in Figure 2 without dismantling the battery from the setup. A current booster which is controlled by an impedance analyzer is added to the system for the high current cycling. A script is written to sequence these experiments without interruption between steps. During EIS tests and aging procedure, battery is submerged in a temperature controlled water bath inside an incubator to keep the temperature constant at 25 °C.

Figure 2. Experimental setup.

2.1. Impedance Analysis Procedure

A 12 V EFB sample is used for a series of impedance analysis. Before starting a test, the battery is charged according to EN 50342-1 CENELEC standard [20]. Following the charging step, 24-h pause period is given for voltage relaxation. Impedance analysis is realized under zero DC to keep the SOC level of the battery constant during the measurements especially at low frequencies. The root mean square of the excitation current is set to $I_n/5$ where I_n equals to a nominal discharge current which can deplete the battery in 20 h. AC signal starts from 10^4 Hz and goes down to 10^{-3} Hz where the frequency step is set as 10 points per decade (PPD) of frequency. For each frequency point; an AC signal (PPF) is applied to the battery for three times of the period to avoid coincidental fluctuations on the voltage response. After each impedance analysis set, the SOC of the battery is decreased 10% by discharging with I_n for 2 h. Following the discharge step, another rest period is given for the voltage relaxation of the battery and the next impedance analysis starts when open circuit voltage change is less than 1 mV/min. This procedure continues down to 20% SOC value and after that, the battery is charged with the same standard. By applying this procedure, the impedance data of the battery is collected for all SOC values at a wide frequency spectrum for a certain SOH.

2.2. Battery Ageing Procedure

After series of an EIS test for a certain SOH value, the battery is aged with respect to micro-hybrid partial cycling standard EN 50342-6 [21]. In this procedure, battery's SOC is decreased to 50% before beginning the cycling. Following the initial discharge, the battery is cycled between 50% and 67.5% SOC values with $7 \times I_n$ charge and discharge currents according to 17.5% endurance cycling procedure. This microcycle is repeated 85 times and it is considered as one unit of aging. During the battery

aging, test termination criterion is the battery voltage, which should be higher than 10 V during the discharging step. After each aging unit, EIS tests are conducted again to understand the change of Z_{Re}, Z_{Im} and phase shift of the battery at different SOH levels. The flowchart of the applied impedance analysis and the aging procedure is given in Figure 3. Experiments are carried on till the voltage decreases to 10 V at cycling unit 10.

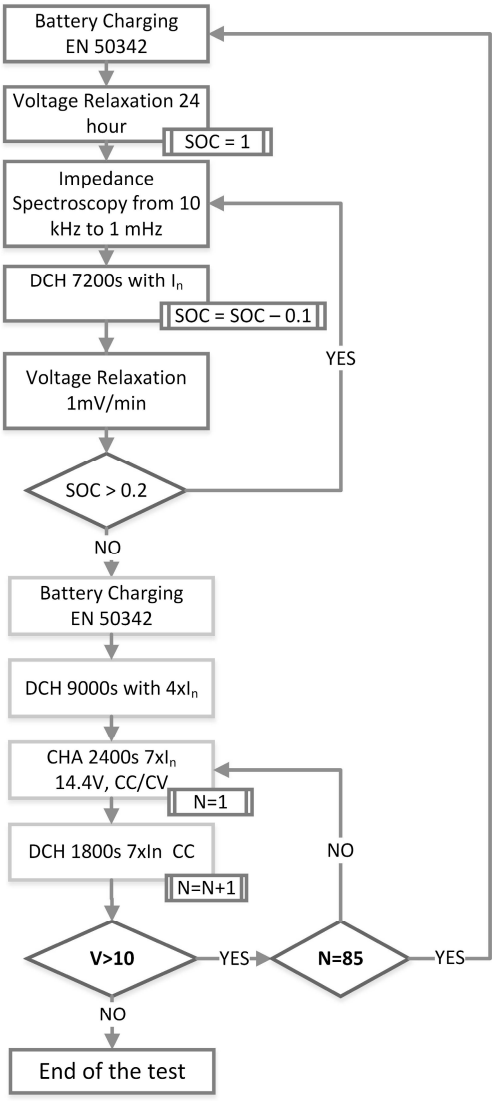

Figure 3. Battery ageing and electrochemical impedance spectroscopy (EIS) procedure.

2.3. Results and Discussion

Impedance analysis for a certain SOH is consecutively repeated with decreasing SOC values as explained in the previous section. Nyquist plots for different SOC values of a new battery are given in Figure 4a, at a range of 10 kHz to 1 mHz. Higher frequency region of the same graph is given in Figure 4b. Battery impedance starts with an inductive behavior at the higher frequency region and as frequency decreases the inductive component is first compensated than surpassed by the capacitive components of the battery.

EIS results of the highest SOC test differ from the rest with its vastly increasing real and imaginary parts seen in Figure 4a. The situation becomes comprehensible since the AC signal acts almost like DC at such low frequencies in the mHz range. During the positive semi-cycle of the impedance signal, the current signal causes to overcharge of an already fully charged battery. This leads to a much

strong voltage increment than those of others. This situation continues for all SOH values at their full SOC levels.

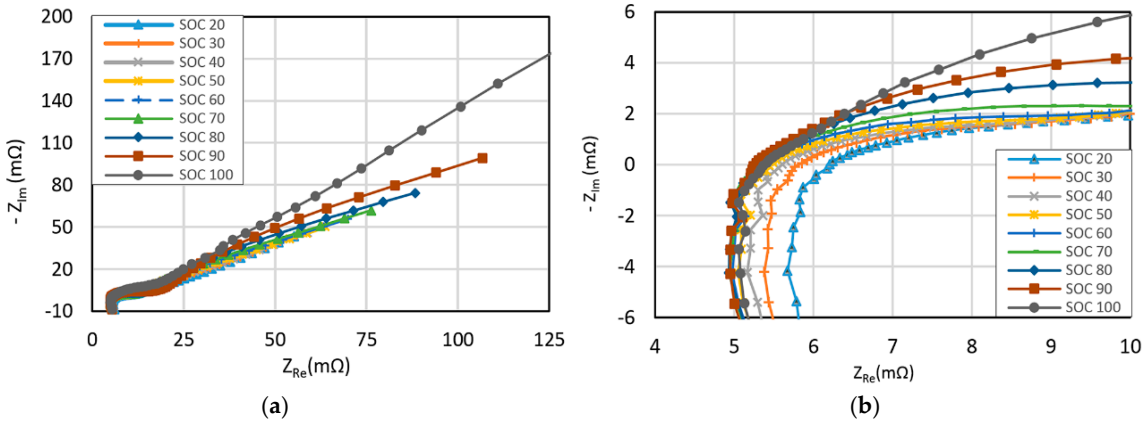

Figure 4. (**a**) Nyquist of a new battery at various states of charge (SOC); (**b**) A detailed view of the high frequency region.

In the early stage of lifetime, increments of real resistance (Z_{Re}) at transition frequency (F_{Tr}) with decreasing SOC levels are limited. Z_{Re} shows less than 1 mΩ increment from 5.38 mΩ to 6.20 mΩ respect to 80% nominal capacity discharge. This is a result of decreasing conductivity of the electrolyte due to sulphuric acid consuming double sulphation reaction. In order to show the aging effect on the battery impedance, EIS data at various SOC levels of the same battery are obtained after five units of micro cycles which decreases the battery state of health to 50%. The results of these experiments are shown in Figure 5a,b.

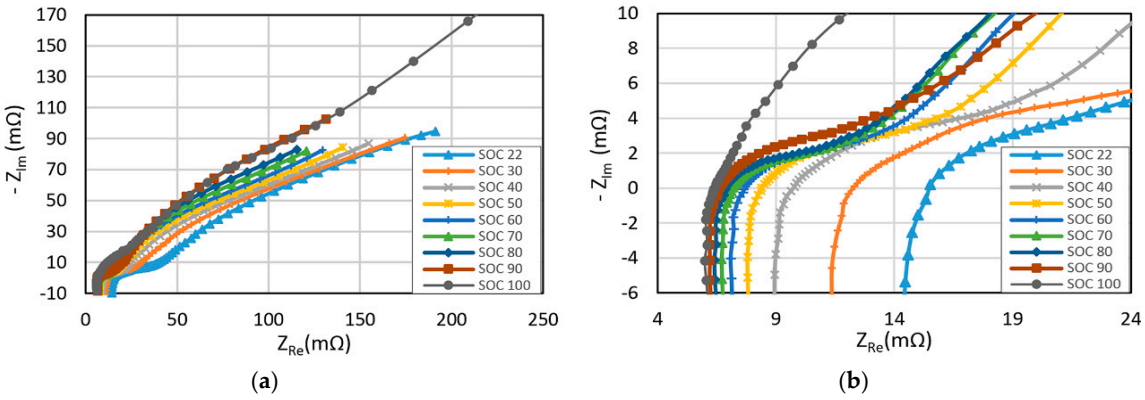

Figure 5. (**a**) Nyquist of a battery at 50% state of health (SOH) at various SOC; (**b**) A detailed view of the high frequency region.

Between these two different health states, Z_{Re} of the battery shows a minimal increment of 0.36 mΩ in their full SOC values. The resistance gap between new and old batteries increases while SOC decreases. At 30% SOC, Z_{Re} of the new battery is 5.81 mΩ where it increases to 11.99 mΩ after 5 units of micro cycling for the same SOC value. The changes of Z_{Re} for an EFB battery under a controlled aging procedure are given in Figure 6. It is seen that the increase in the DC resistance is minimal at all SOH levels at higher SOC region till there is a malfunction in the battery at the end of its lifetime. On the other hand, the increase in the resistance at the lower SOC region is highly remarkable.

During the change of SOC from 100% to 30%, it is observed that Z_{Re} increases only 7.9% for a new battery (100% SOH) while it increases 108% and 162% for 50% SOH and 10 % SOH respectively. At the end of 10th ageing unit, battery voltage decreases below 10 V and the test is over. At that point,

SOH is assumed 0% and the battery is fully charged again to do a final test of EIS thorough out the capacity remains.

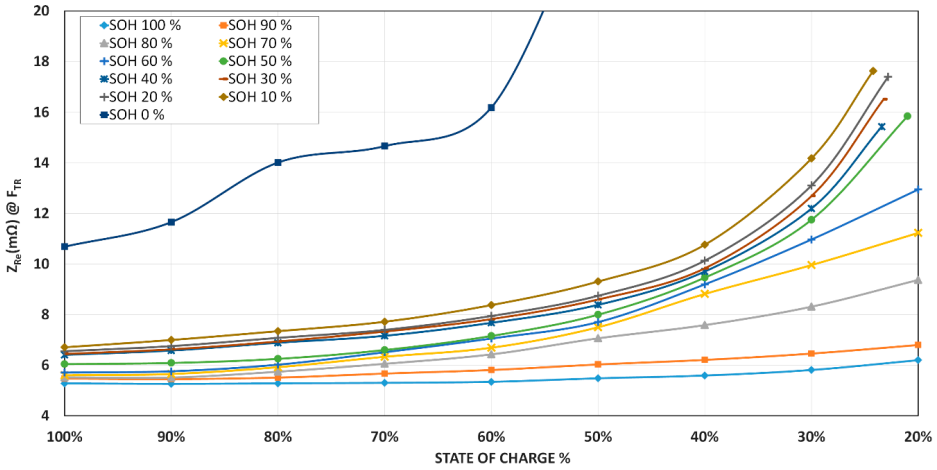

Figure 6. Change of internal resistance with SOC at various SOH levels.

3. Model Accordance Comparisons of EEC Models with Data for Different SOC and SOH Conditions

EIS graphs gives a lot of information and clues about the electrochemical processes in a battery if interpreted with an EEC where the elements have physical meaning and have a good match with data. To extract the useful information and make predictions for SOC and SOH from these data, an electric circuit model, which mimics the essential dynamics of a battery, is needed. Four different models are applied for gathered EIS data to analyze their consistency through a broad spectrum range for an EFB.

EEC models consist only from simple electric elements have been considered in the literature both for lead acid batteries [22,23] and for other chemistries [13,27–29] as well. In addition to SOC and SOH estimations there are applications of these models as a thermal model for batteries [30]. On the bright side, these models require less computational power, thus less time to give a prediction and have a good consistency with data on the higher frequency range if they have a serial inductance. They can be used to mimic the voltage response of batteries for a given load using parallel with a coulomb counting based SOC calculator. On the other hand, their impedance response consistency with respect to data are lower than those of other models because of difficulties in describing the electric characteristics of diffusion mechanisms by conventional elements. Thus, as the excitation signal frequency decreases model consistency with the data decreases. Further studies such as neural network training [23] or variances of Kalman filtering [11] for that type of EEC's have been developed to decrease the model error margin. A simple element model is seen in Figure 6a.

A Randles cell, shown in Figure 7B, also finds approval to interpret lead acid batteries [24]. Elements of the circuit cover the essential dynamics of a lead acid battery. A serial resistance for the frequency independent parts like separator and electrolyte resistances, an inductance for all the high frequency metallic components, a parallel capacitor for the electrochemical double layer effect, a parallel resistance for the faradaic reactions that occur on the electrode's surface and a Warburg element for the diffusion related mass transport limitation processes of the battery.

The non-ideal capacitive behavior of an electrode appears with suppressed semi-circles on the Nyquist plot of EFB. It is hard to imitate this behavior with parallel RC circuit. Model A has been modified by using a constant phase element (CPE), which is a capacitor with a leakage parameter of α. Impedance expression of CPE is given as:

$$Z_{\mathrm{CPE}} = \frac{1}{C(i\omega)^{\alpha}} \tag{3}$$

if $\alpha = 1$ then CPE element becomes a pure capacitor. When α goes to 0, it behaves like a resistor [31]. This EEC has been used in several works [19,25] to get a more accurate electrode behavior of lead acid batteries compared to first two models.

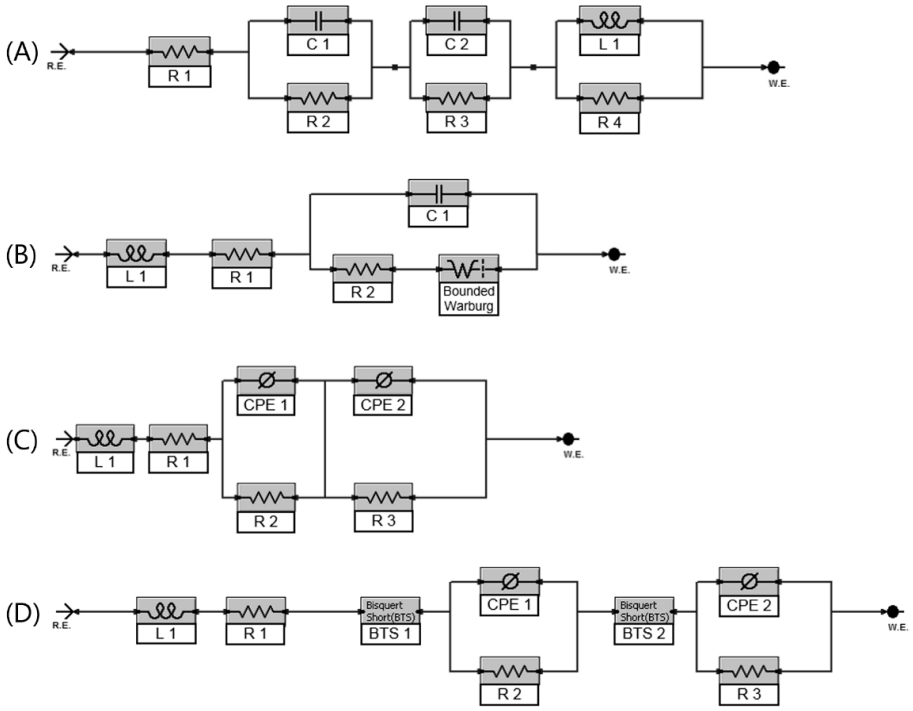

Figure 7. (**A**) Electric equivalent circuit (EEC) consisted from simple electric circuit elements R, L and C; (**B**) EEC of a Randles Circuit with a serial inductance; (**C**) EEC with constant phase elements (CPEs); (**D**) EEC with CPE and transmission line elements.

High electrode surface area is a key parameter to get a high power and dynamic charge acceptance as well as low internal resistance. New and highly porous active materials have been developed in lead acid market and applied on EFB as well as other electrochemical power sources. EEC models, which consider the electrode-electrolyte interface as a planar surface, are based on an assumption that the reaction occurs directly on the surface of the electrode. For a porous electrode surface, however, ion diffusion parameters depend on electrolyte concentration and it changes as ion penetrates into the deeper part of pores. Due to continuous parameter changes through the pore, ion diffusion and charge transfer parameters are modelled with infinite number of elements. An illustration of a transmission line element for ion flux inside a pore is given in Figure 8.

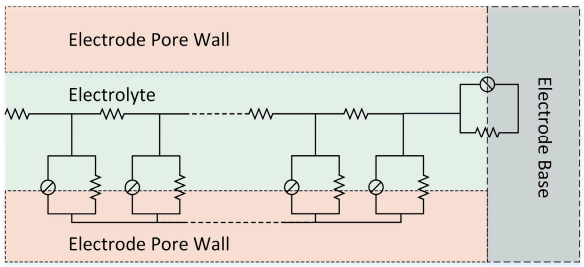

Figure 8. Transmission line elements inside a pore.

The impedance of such a transmission line element for porous electrodes on different media has been calculated in the literature before [32]. Theory explained in that work has been applied

from super capacitors to dye-sensitized solar cells and many other applications where diffusion and recombination processes occur.

Due to the nature of lead acid battery chemistry the substrate surface is not isolated and interacts with the electrolyte. Thus, a transmission element, which also includes interactions on the pore bottom, is considered here. The widely used EEC in Figure 7C is modified by adding a transmission line element and the model given in Figure 7D is proposed for an EFB for the first time. The results and accuracy of the proposed model with those of other EEC models are compared by following the Kramer-Kronig validation of each data set.

EEC models are applied to experimental data by a commercial software based on simplex algorithm which tries to minimize the χ^2 value between data and model prediction. χ^2 is defined as:

$$\chi^2 = \sum_{i=1}^{71} w_i \left[\left(Z_{re(data)} - Z_{re(model)} \right)^2 + \left(Z_{im(data)} - Z_{im(model)} \right)^2 \right] \quad (4)$$

where number of data is 71 and w_i is:

$$w_i = \frac{1}{\sqrt{\left(Z_{re(data)} \right)^2 + \left(Z_{im(data)} \right)^2}} \quad (5)$$

Nyquist and bode diagrams shown in Figure 9a,b are given to demonstrate the accuracy of data fitting of various EEC models. The graph belongs to the battery almost at the end of its life (20% SOH) and 80% SOC level. It is seen that without applying a further improvement technique, a simple circuit model (Model A) is not able to express the electrochemical phenomena on an EFB especially for the lower frequencies. A Randles circuit with a CPE (Model B) has a good agreement with data at the higher frequency region though its accuracy decreases sharply below 1 Hz. The third EEC model, which has a serial resistance and an inductance connected to two parallel R—CPE elements (model C) to represent both electrodes, has much better compliance with the experimental results in comparison with model A and model B for the whole frequency range from 10 kHz to 1 mHz. In the fourth and final EEC model, transmission line inclusion to both electrodes (model D) decreases the discrepancy between the data and the model further.

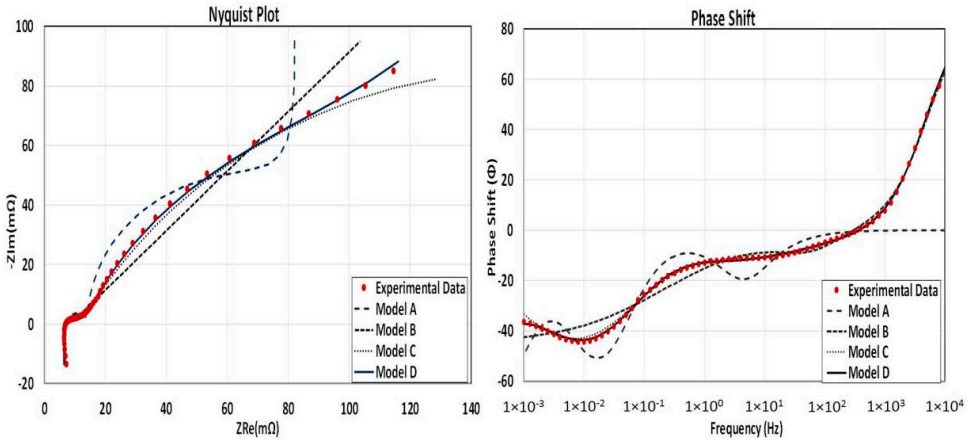

(**a**) (**b**)

Figure 9. (**a**) Nyquist and (**b**) Bode diagrams of the electrochemical impedance spectroscopy (EIS) data and model compatibility for 80% SOC and 20% SOH.

To make a quantitative comparison on the accuracies of the models, all three measured parameters Z_{Re}, Z_{Im}, and the phase angle Φ are compared with those of each model based on mean absolute percentage error (MAPE) method. MAPE calculations of Z_{Re}, Z_{Im}, and Φ are given in Equations (6)–(8), respectively.

$$\mathrm{MAPE}(Z_{Re}) = \frac{1}{N}\sum_{i=1}^{N}\frac{|Z_{re(data)} - Z_{re(model)}|}{|Z_{re(data)}|} \quad (6)$$

$$\mathrm{MAPE}(Z_{Im}) = \frac{1}{N}\sum_{i=1}^{N}\frac{|Z_{im(data)} - Z_{im(model)}|}{|Z_{im(data)}|} \quad (7)$$

$$\mathrm{MAPE}(\Phi) = \frac{1}{N}\sum_{i=1}^{N}\frac{|\Phi_{data} - \Phi_{model}|}{|\Phi_{data}|} \quad (8)$$

MAPE values of Z_{Re}, Z_{Im}, and Φ are given in Figure 10, for all four models.

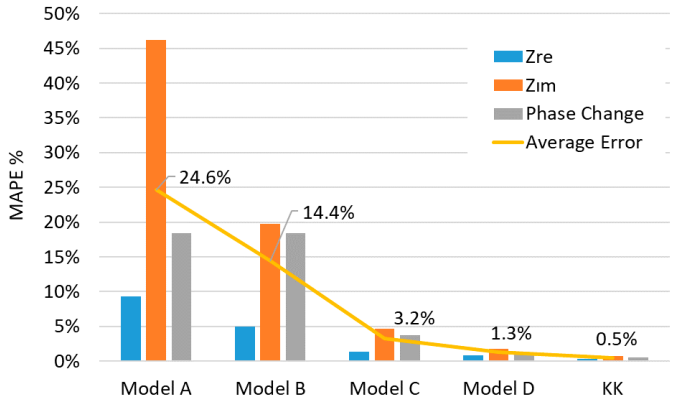

Figure 10. The mean average percentage error (MAPE) values of Z_{Re}, Z_{Im}, and Φ for different EEC models at 80% SOC and 20% SOH.

Model A has a compatibility with the data only for a limited range. Although it can start with a matching real resistance, lacking a serial inductance prevents it to handle the positive imaginary part of the data for the high frequency part. Parallel R-C and R-L parts are trying to form two semi-circles and a sharp diffusion behavior which could not cover the data well enough in most circumstances. Similar model-data mismatch continues for the phase shift at the high frequency range and resulting a bigger average MAPE value than other models which is 24.6% as can be seen in Figure 8. Model B can cover the data with a good match for the high frequency region with a resistance inductance couple in series but highly linear response of the second part decreases the model compatibility as the frequency decreases. Model C, which is extensively used in literature, can cover the data with 3.2% average value of MAPE and has a good adaptation to the data through the whole frequency spectrum. Similar to the previous model, its serial resistance and inductance elements can handle the high frequency spectrum while two ZARCs in series are matching well enough to model the data on lower frequency range. Adding transmission line elements prior to each ZARC element on Model C decreases the error margin even further down to 1.3%, which is shown in Model D.

Data fitting procedure is applied to 11 different SOH level for nine different SOC conditions as explained in Figure 1. Prior to each fitting trial, Kramers-Kronig (KK) test is applied to the gathered data. Except the fully charged states, KK can track data with a goodness of fit value of less than 8×10^{-6} which indicates the reliability of data sets. At 100% SOC levels data solidity decreases because of the overcharging behavior of the lower frequency signal deteriorates the Lissajous curves. Beside that state of charge, KK values are always lower than 1% error range for all three measured parameters. Variations of MAPE values for all four models throughout the whole SOC range as the SOH decreases are given in Figure 11. It is seen that Model D, with transmission line elements, preserves its lower error margin and the accuracy is always higher than those of other models.

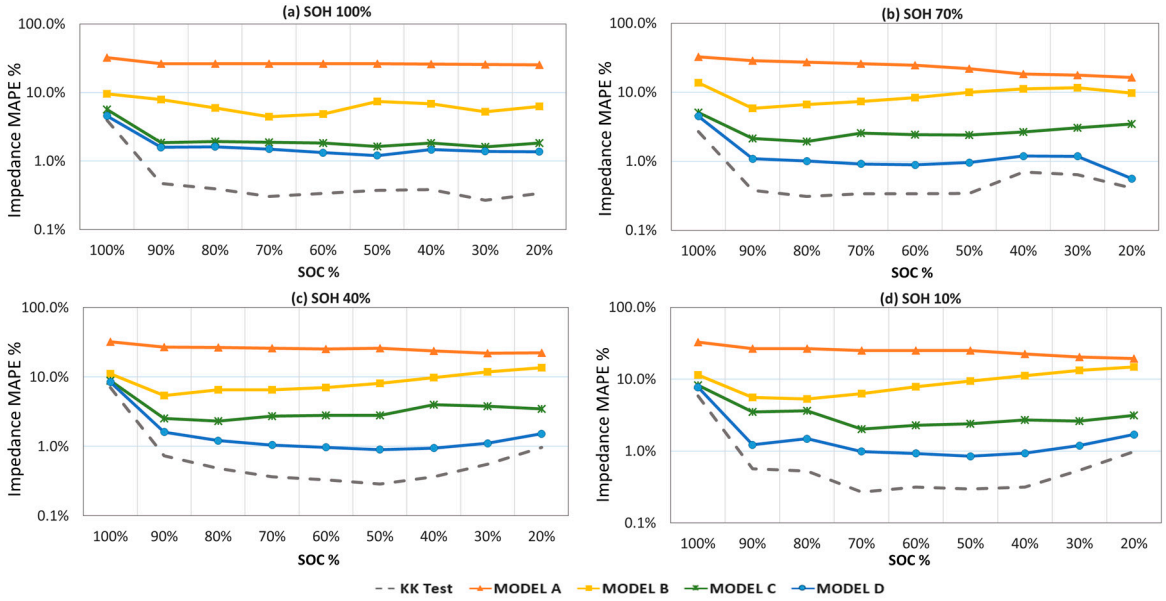

Figure 11. Variation of MAPE values with SOC % for different models at: (**a**) SOH 100%; (**b**) SOH 70%; (**c**) SOH 40%; and (**d**) SOH 10%.

Based on the averaged MAPE value of all SOC values for a certain SOH, four models and KK values are compared with respect to each other in Figure 12. Depending on data quality based on KK results, the averaged MAPE values of Model D over SOC vary from 1.0% to 3.4% for different SOH values and gives 1.6% double averaged result over SOH while the double averaged value of KK is about 0.8%. On the other hand, the Model C can represent the impedance data with 3.2% double averaged MAPE over whole SOC and SOH ranges. The same quantity is 24.7% and 8.9% for Model A and Model B, respectively.

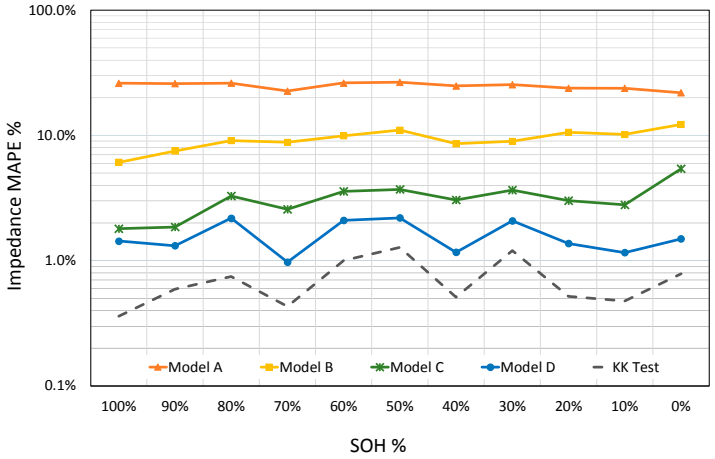

Figure 12. Variation of average MAPE values with SOH for different EEC models.

4. Conclusions

An enhanced lead-acid battery with increased cold cranking performance and cycle life is examined by EIS for a wide range of SOH and SOC conditions. Charge, discharge, and aging procedures defined for micro hybrid vehicle batteries are applied to the battery. Changes of resistance are also recorded for these various SOC and SOH steps through the lifetime of the battery. It is observed that increment of resistance between fully charged and empty states is limited by 7.9% for a new

battery. This increment boosts to 162% when the battery reaches to the end of its life. Although there is a correlation between resistance and SOC, this correlation can only be used for SOC estimation if there is a certain knowledge about the SOH of the battery.

Four EEC models are applied to the impedance data gathered. Consistencies of models with data are examined for a broad SOH and SOC range. It is shown that the proposed model with transition line elements has better accuracy in comparison with those of other models. Although degree of freedom and computing time increase due to additional elements in the model, this problem is trivial for today's modern computers. The marginal benefit of the model with transmission line element becomes evident as the battery's SOH decreases. The double averaged MAPE value is only 1.6% for Model D while the Model C has 3.2%. As a result of this work, it is seen that enhanced flooded lead acid batteries with higher porosity electrodes can be simulated better through the frequency spectrum from 10 kHz to 1 mHz with transmission line element included EEC models. These models have a potential for a better SOC and SOH predictions and they may represent more realistic battery behaviors in complex simulation environments.

For future works, an EFB battery at different health and charge states will be tested on a test bench which can simulate high charge and discharge currents of an alternator under real driving conditions of a micro hybrid vehicle. The time domain results of the proposed model with transmission line element will be compared with those results.

Acknowledgments: This project is supported by INCI GS YUASA Battery Company and the Republic of Turkey, Ministry of Science, Industry, and Technology under contract number of 00552.STZ.2010-1 and authors are thankful to Burak Ulgut from Bilkent University Chemistry Department for a series of seminal discussions.

Author Contributions: Can Aksakal conceived, designed, and performed the experiments; Can Aksakal and Altug Sisman have analyzed the data and wrote the paper together.

Conflicts of Interest: The authors declare no conflict of interest.

Nomenclature

C	Capacitance (F)
C_n	nominal capacity (Ah)
F_{TR}	Transition Frequency (Hz)
i	Imaginary unit
I_n	nominal discharge current (A) (C_n/20 h)
R_i	internal resistance (Ω)
U_c	charging voltage (V)
χ^2	Chi-square
ω	Radial Frequency
Z_{Re}	real impedance (Ω)
Z_{Im}	imaginary impedance (Ω)
Φ	Phase Shift

Abbreviations

AGM	Absorbed Glass Mat
CHA	Charge
DCH	Discharge
DOD	Depth of Discharge
EEC	Electric Equivalent Circuit
EFB	Enhanced Flooded Battery
EIS	Electrochemical Impedance Spectroscopy
KK	Kramers-Kronig
MAPE	Mean Absolute Percentage Error
SLI	Starting Lighting Ignition
SOC	State of Charge (%)
SOH	State of Health (%)

References

1. EU CO_2 Emission Standards for Passenger Cars and Light Commercial Vehicles. Available online: http://www.theicct.org/sites/default/files/publications/ICCTupdate_EU-95gram_jan2014.pdf (accessed on 17 August 2017).
2. Navigant Research Global Market Analysis and Forecast Report on Stop-Start Vehicles. Available online: https://www.navigantresearch.com/newsroom/sales-of-stop-start-vehicles-will-surpass-55-million-units-annually-by-2022 (accessed on 28 September 2017).
3. Karden, E.; Warm, A.; Rymond, R.; Nagata, Y.; Shinn, P. Lead/Acid batteries for automotive applications—New requirements and ongoing innovation. In Proceedings of the 14th ELBC European Lead Battery Conference, Edinburg, UK, 9–14 September 2014.
4. Budde-Meiwes, H.; Drillkens, J.; Lunz, B.; Muennix, J.; Rothgang, S.; Kowal, J.; Sauer, D.U. A review of current automotive battery technology and future prospects. *Proc. Inst. Mech. Eng. Part D J. Automob. Eng.* **2013**, *227*, 761–776. [CrossRef]
5. Pavlov, D.; Nikolov, P. Capacitive carbon and electrochemical lead electrode systems at the negative plates of lead–acid batteries and elementary processes on cycling. *J. Power Sources* **2013**, *242*, 380–399. [CrossRef]
6. Moseley, P.T.; Rand, D.; Peters, K. Influence of some nanostructured materials on the performance of lead acid battery negative electrodes. *Electrochim. Acta* **2014**, *144*, 147–153.
7. Nakhaie, D.; Benhangi, P.H.; Alfantazi, A.; Davoodi, A. The effect of grid configurations on potential and current density distributions in positive plate of lead–acid battery via numerical modeling. *Electrochim. Acta* **2014**, *115*, 189–196. [CrossRef]
8. YUASA AGM & EFB Automotive Batteries Explanation Webpage. Available online: https://www.yuasa.co.uk/info/technical/agm-efb-explained/#efb (accessed on 28 September 2017).
9. VARTA EFB Enhanced Technology Explanation Webpage. Available online: https://www.varta-automotive.com/en-gb/technology/efb-battery-technology (accessed on 28 September 2017).
10. BOSCH Enhanced Flooded Battery Technology Explanation Webpage. Available online: http://za.bosch-automotive.com/en_GB/parts_and_accessories_2/service_parts_1/batteries_4/batterietechnologien_1/efb/efb_1 (accessed on 28 September 2017).
11. Tran, N.; Khan, A.B.; Choi, W. State of charge and state of health estimation of AGM VRLA batteries by employing a dual extended kalman filter and an ARX model for online parameter estimation. *Energies* **2017**, *10*, 137. [CrossRef]
12. Tenno, A.; Tenno, R.; Suntio, T. A method for battery impedance analysis. *J. Electrochem. Soc.* **2004**, *151*, A806–A824. [CrossRef]
13. Gao, Z.; Chin, C.S.; Woo, W.L. Lithium-ion battery modeling and validation for the smart power system. In Proceedings of the IEEE International Conference on Computer, Communications, and Control Technology (I4CT), Kuching, Malaysia, 21–23 April 2015; pp. 269–274.
14. Zou, C.; Hu, X.; Wei, Z.; Tang, X. Electrothermal dynamics-conscious lithium-ion battery cell-level charging management via state-monitored predictive control. *Energy* **2017**, *141*, 250–259. [CrossRef]
15. Zou, C.; Manzie, C.; Neši´c, D. A framework for simplification of PDE-based LITHIUM-Ion battery models. *IEEE Trans. Control Syst. Technol.* **2016**, *24*, 1594–1609. [CrossRef]
16. Tsividis, Y.; Milios, J. A detailed look at electrical equivalents of uniform electrochemical diffusion using nonuniform resistance-capacitance ladders. *J. Electroanal. Chem.* **2013**, *707*, 156–165. [CrossRef]
17. Gopikanth, M.L.; Sathyanarayana, S. Impedance parameters and the state-of-charge. II. Lead-acid battery. *J. Appl. Electrochem.* **1979**, *9*, 369–379. [CrossRef]
18. Mauracher, P.; Karden, E. Dynamic modeling of lead/acid batteries using impedance spectroscopy for parameter identification. *J. Power Sources* **1997**, *67*, 69–84. [CrossRef]
19. Blanke, H.; Bohlen, O.; Buller, S.; de Doncker, R.W.; Fricke, B.; Hammouche, A.; Linzen, D.; Thele, M.; Sauer, D.U. Impedance measurements on lead–acid batteries for state-of-charge, state-of-health and cranking capability prognosis in electric and hybrid electric vehicles. *J. Power Sources* **2005**, *144*, 418–425. [CrossRef]
20. European Committee for Electrochemical Standardization. *Lead-Acid Starter Batteries—Part 1: General Requirements and Methods of Test*; Standard BS EN 50342-1; CEN: Brussels, Belgium, 2006.
21. European Committee for Electrochemical Standardization. *Lead-Acid Starter Batteries—Part 6: Batteries for Micro-Cycle Applications*; Standard BS EN 50342-6; CEN: Brussels, Belgium, 2015.

22. Salkind, A.J.; Singh, P.; Cannone, A.; Atwater, T.; Wang, X.; Reisner, D. Impedance modeling of intermediate size lead–acid batteries. *J. Power Sources* **2003**, *116*, 174–184. [CrossRef]
23. Monfared, N.A.; Gharib, N.; Moqtaderi, H.; Hejabi, M.; Amiri, M.; Torabi, F.; Mosahebi, A. Prediction of state-of-charge effects on lead-acid battery characteristics using neural network parameter modifier. *J. Power Sources* **2006**, *158*, 932–935. [CrossRef]
24. White, C.; Deveau, J.; Swan, L.G. Evolution of internal resistance during formation of flooded lead-acid batteries. *J. Power Sources* **2016**, *327*, 160–170. [CrossRef]
25. Zhu, W.H.; Zhu, Y.; Bruce, J.; Tatarchuk, B.J. A simplified equivalent circuit model for simulation of Pb–acid batteries at load for energy storage application. *Energy Convers. Manag.* **2011**, *52*, 2794–2799. [CrossRef]
26. Boukamp, B.A. A linear Kronig-Kramers transform test for immittance data validation. *J. Electrochem. Soc.* **1995**, *142*, 1885–1894. [CrossRef]
27. Safwat, I.M.; Li, W.; Wu, X. A novel methodology for estimating state-of-charge of Li-Ion batteries using advanced parameters estimation. *Energies* **2017**, *10*, 1751. [CrossRef]
28. Jung, S.; Jeong, H. Extended kalman filter-based state of charge and state of power estimation algorithm for unmanned aerial vehicle Li-Po battery packs. *Energies* **2017**, *10*, 1237. [CrossRef]
29. Jia, J.; Lin, P.; Chin, C.S.; Toh, W.D.; Gao, Z.; Lyu, H.; Cham, Y.T.; Mesbahi, E. Multirate strong tracking extended kalman filter and its implementation on lithium Iron Phosphate (LiFePO4) battery system. In Proceedings of the 11th IEEE International Conference on Power Electronics and Drive Systems (PEDS), Sydney, Australia, 9–12 June 2015; pp. 640–645.
30. Gao, Z.; Chin, C.S.; Woo, W.L.; Jia, J. Integrated equivalent circuit and thermal model for simulation of temperature-dependent LiFePO4 battery in actual embedded application. *Energies* **2017**, *10*, 85. [CrossRef]
31. Zou, C.; Hu, X.; Dey, S.; Zhang, L.; Tang, X. Nonlinear fractional-order estimator with guaranteed robustness and stability for Lithium-Ion batteries. *IEEE Trans. Ind. Electron.* **2017**, *PP*, 1. [CrossRef]
32. Bisquert, J. Influence of the boundaries in the impedance of porous film electrodes. *Phys. Chem. Chem. Phys.* **2000**, *2*, 4185–4192. [CrossRef]